Atmos. Chem. Phys. Discuss., 12, 17503–17538, 2012
www.atmos-chem-phys-discuss.net/12/17503/2012/
doi:10.5194/acpd-12-17503-2012

Atmospheric Chemistry and Physics Discussions

Identification of key aerosol populations through their size and composition resolved spectral scattering and absorption

F. Costabile, F. Barnaba, F. Angelini, and G. P. Gobbi

Institute for Atmospheric Sciences and Climate, National Research Council (ISAC-CNR), Rome, Italy

Received: 11 June 2012 – Accepted: 1 July 2012 – Published: 17 July 2012

Correspondence to: F. Costabile (f.costabile@isac.cnr.it)

Published by Copernicus Publications on behalf of the European Geosciences Union.

Abstract

Characterizing chemical and physical aerosol properties is important to understand their sources, effects, and feedback mechanisms in the atmosphere. This study proposes a scheme to classify aerosol populations based on their spectral optical properties (absorption and scattering). The scheme is obtained thanks to the outstanding set of information on particle size and composition these properties contain. The spectral variability of the aerosol Single Scattering Albedo (dSSA), and the Scattering and Absorption Angstrom Exponents (SAE and AAE, respectively) were observed on the basis of two-year measurements of aerosol optical properties (scattering and absorption coefficients at blue, green and red wavelengths) performed in the suburbs of Rome (Italy). Optical measurements of various aerosol types were coupled to measurements of particle number size distributions and relevant optical properties simulations (Mie theory). These latter allowed to investigate the role of the particle size and composition in the bulk aerosol properties observed. The combination of simulations and measurements suggested a general "paradigm" built on dSSA, SAE and AAE to optically classify aerosols. The paradigm proved suitable to identify the presence of key aerosol populations, including soot, biomass burning, organics, dust and marine particles. The work highlights that: (i) aerosol populations show distinctive combinations of SAE and dSSA times AAE, these variables being linked by a linear inverse relation varying with varying SSA; (ii) fine particles show SAE > 1.5, whilst SAE < 1 is found for both coarse particles and ultrafine soot-rich aerosols; (iii) fine and coarse particles both show SSA > 0.8, whilst ultrafine urban Aitken mode and soot particles show SSA < 0.8. A strict agreement was found when comparing the proposed paradigm to aerosol observations performed during past major field campaigns.

ACPD

12, 17503–17538, 2012

1 Introduction

Aerosol particles play a central role in the atmosphere. Small variations of their chemical and physical properties generate significant feedback mechanisms with complex and combined impacts ranging from local air pollution and related health effects (WHO, 2003) to global climate (IPCC, 2007). Variations of their optical properties and capability to act as CCN are determinant for the climatic (direct and indirect, respectively) impact.

Tropospheric aerosols may contain carbonaceous material, sulfate, nitrate, ammonium, trace metals, sea salts, crustal elements, their sizes spanning over more than four orders of magnitude, from few nanometers to several micrometers (e.g. Seinfeld and Pandis, 2006). Particle sizes and composition together with their mixing state and shape identify aerosol populations, each of them having specific chemical, optical and physical properties, as well as sources and sinks, space-scales and lifetime. Whilst aerosol mass is dominated by the "coarse" (particle diameter, D_p from 1.0 to 10 µm) and fine ($D_p < 1.0$ µm, the "accumulation" mode) particles, their number is dominated by the ultrafine particles (UFP, $D_p < 100$ nm) in the "nucleation", and "Aitken" mode ($D_p < 50$ nm, 50–100 nm, respectively). The size resolved understanding of the particle numbers, and in particular of the carbonaceous aerosols, is among the major knowledge gaps to assess the impact of air pollution on climate (Kulmala et al., 2011).

Carbonaceous aerosols include black carbon (BC) and organic material (OM), and represent most of the anthropogenic aerosol in terms of both mass and number concentrations. BC in the lower atmosphere is the major absorbing component of atmospheric aerosol and a harmful air pollutant that has both substantial regional and global climate impacts, and adverse human health effects (UNEP, 2011). Recently, Reche et al. (2011) demonstrated that between 3 and 20 % of PM_{10} at several European urban sites is due to BC. Conversely, OM has been thought to have a cooling effect (i.e., negligible absorption properties); some organic compounds, however, have been found to absorb light in the UV and visible

ACPD
12, 17503–17538, 2012

(Kirchstetter et al., 2004; Andreae and Gelencsér, 2006), and have therefore been referred to as "Brown Carbon" (Andreae and Gelencsér, 2006; Alexander et al., 2008). The brown carbon, a subset of the whole organic carbon, exhibits a strong wavelength (λ) dependent absorption in the UV and visible, which is larger at near-UV and blue wavelengths (Sun et al., 2007). Jacobson (2001) identified nitrated and aromatic compounds as likely absorbers. Bond (2001) suggested different levels of aromatization to explain the particle absorption spectral variability. So far a complete knowledge of the nature of brown carbon remains indefinite.

The wavelength dependence of the light absorption is crucial to evaluate the spectral single scattering albedo (SSA) (Bergstrom et al., 2007; Russell et al., 2010), a key parameter in the evaluation of the aerosol (direct) climate forcing. Bergstrom et al. (2007) showed that the absorption coefficient decreases monotonically with wavelength and can be approximated by a power-law expression, i.e. described by an Absorption Angstrom Exponent (AAE). The slope of this decrease (or the value of AAE) strongly depends on the aerosol characteristics. Although crucial, it is actually quite difficult to accurately measure the absorption resolved by wavelength, particle size, shape, composition and internal mixing state. In addition, a lack of a generally accepted reference or calibration standard for the aerosol absorption coefficient remains (e.g. Moosmüller et al., 2009). As a consequence, the spectral variability of both light absorption and SSA is still poorly determined and bears a large uncertainty.

In the past, much attention has been devoted to the spectral variability of the light scattering and extinction (quantified by the Scattering and Extinction Angstrom Exponents, SAE and EAE). SAE and EAE data have been analyzed by several authors to classify aerosol types in terms of particle size (e.g. O'Neill et al., 2001a,b; Gobbi et al., 2007). Gobbi et al. (2007) proposed a graphical method to gain information on the relevant extinction and the size of the fine aerosols based on the EAE and its spectral curvature. The method, applied to AERONET data (Holben et al., 1998), allowed for easy identification of some aerosol type fingerprints (e.g. mineral dust, pollution) (Basart et al., 2009). Combination of extinction or scattering (EAE or SAE) and absorption

ACPD
12, 17503–17538, 2012

(AAE) spectral variability is becoming more and more used to infer aerosol composition from optical data (e.g. Bergstrom et al., 2007; Clarke et al., 2007; Yang et al., 2009; Gyawali et al., 2012; Lee et al., 2012). Clarke et al. (2007) used the analysis of SAE and AAE to distinguish between dust, biomass burning and urban aerosol in airborne in situ data. Yang et al. (2009) used SAE versus AAE for Beijing, and separated dust (generally SAE close to zero and AAE variable, but high), fresh plumes (AAE around 1), and coal pollution (more variable AAE because of the formation of brown carbon). Gyawali et al. (2012) clearly separated clean days from polluted days by combining AAE and SAE with SSA.

The spectral variability of SSA (dSSA/dλ) has been also proposed as an indicator of particle size. Ackerman and Toon (1981) found that positive dSSA/dλ can be caused by the domination of the coarse particle mode in the aerosol size distribution. Bergstrom (1973) showed that for atmospheric aerosols that do not contain large particles, SSA of the mixture decreases with λ. Several authors have investigated the dependence of dSSA/dλ on aerosol composition. Kaufman et al. (2001) showed that SSA for dust increases with increasing λ because of the absorption in the blue channels due to the presence of iron oxides in hematites. Dubovik et al. (2002) obtained dSSA/d$\lambda < 0$ for urban pollution and smoke aerosols. Bergstrom et al. (2002) proposed the use of the spectral SSA variability to differentiate between dust and BC absorption. Russell et al. (2010) analysed SSA and AAE in AERONET and in situ data, and concluded that information on aerosol type cannot come from the wavelength dependence of absorption only, the particle size information in the scattering wavelength dependence being also needed.

In this work, we observed the spectral aerosol absorption and scattering properties in the visible region at a sub-urban Mediterranean site (Rome) together with particle number size distributions. In situ observations were interpreted on the basis of numerical simulations (Mie theory) to investigate intensive optical properties resolved by particle size and refractive index. The objective was to infer a general classification scheme based on the intensive parameters SAE, AAE, SSA and dSSA coupled to the

ACPD
12, 17503–17538, 2012

particle size information to "optically" separate key aerosol populations including soot, biomass burning, organic, inorganic, dust and marine aerosols.

2 Experimental

In situ aerosol optical properties have been continuously measured at the ISAC Rome Atmospheric Supersite (http://www.diapason-life.eu/images/RAS-LAST.pdf) since October 2010. The site, representative of suburban background conditions with regular advection of Saharan dust (Barnaba and Gobbi, 2004; Gobbi et al., 2004), is located in the southern outskirts of Rome within 5 km from the city boundary and 40 km from the Mediterranean coast. The dataset presented here includes data from October 2010 to March 2012.

An integrating nephelometer (Ecotech, mod.Aurora 3000) was operated to measure the scattering coefficient (σ_s) due to aerosol particles at three wavelengths, 450, 520, 635 nm. A full calibration of the nephelometer was performed regularly one time per season by using CO_2 as span gas. Zero calibration and adjust were performed once a day by using internally filtered particle free air. Raw data provided by the nephelometer, σ_{neph}, were corrected for truncation according to Anderson and Ogren (1998), Bond (2001), and Müller et al. (2011). Briefly, the true scattering coefficient, σ_s, is obtained by $\sigma_s = C \cdot \sigma_{neph}$, with correction factors $C = C(\lambda)$ calculated as $C = a + b \cdot \mathrm{SAE}$. The coefficients $a = a(\lambda)$ and $b = b(\lambda)$ at each wavelength were taken from Müller et al. (2011), with the SAE being calculated starting from the uncorrected nephelometer data σ_{neph}. The results showed larger truncation error for larger σ_s. According to Bond et al. (2009), we estimated a scattering error for truncation of 1–3 %.

A 3-wavelength particle soot absorption photometer (PSAP, Radiance Research) was operated to measure the absorption coefficient, σ_p, at three wavelengths, namely 467, 530, 660 nm. Raw PSAP data were corrected after the iterative procedure described by Bond et al. (1999), Virkkula et al. (2005), and Virkkula (2010). The procedure requires wavelength resolved σ_s, which were extrapolated from the nephelometer

ACPD
12, 17503–17538, 2012

measurements by means of the measured SAE. Since the PSAP correction factors strongly depend on the filter transmittance (Tr), only data with $Tr > 0.7$ are generally used (Bond et al., 1999). However, due to the high aerosol burden at our site the filter gets often loaded in a few hours. We therefore retained PSAP data with $Tr > 0.5$ to increase the data temporal coverage. Overall, the accuracy of the PSAP measurement considering all corrections is estimated on the order of 20–30 % (e.g. Bond et al., 1999; Virkkula et al., 2005; Cappa et al., 2008; Lack et al., 2008). PSAP measurements can be further complicated by the presence of organic species in the liquid state, which can wet the filter material (Subramanian et al., 2007; Lack et al., 2008). In principle, a similar effect can result in the presence of ultrafine liquid particles, as well. PSAP data should be therefore considered as an upper limit of the "true" value.

Total particle number concentration (N) was measured by a Condensation Particle Counter, CPC (TSI, mod.3022A). The lowest cut off particle diameter (D_p) is D_{p50} (50 % of particle detection) at 7 nm, and D_{p90} at 15 nm. The N_7 (total number concentration of particles larger than 7 nm) is up to 10^6 #cm^{-3}.

Additional data resources used in this study include particle number size distribution (PNSD) from 14 nm to 10 µm. PNSDs from 14 nm to 600 nm were measured by a Scanning Mobility Particle Sizer, SMPS (TSI, mod.3936) in the same area and analyzed in a previous work (Costabile et al., 2010). PNSDs from 0.3 to 10 µm were measured by an Optical Particle Counter, OPC (FAI instruments). LIDAR profiles (e.g. Gobbi et al., 2007) and local meteorological parameters were also available and thus used in support to the data interpretation.

In situ measurements were carried out under dry conditions owning to a relative humidity always below 50 % observed in the in situ instruments. Particle losses into the sampling line were calculated according to Hinds (1999), with the sampling inlets removing particles larger than 10 µm and the particle penetration efficiency through the line being >98 % for $D_p > 10$ nm.

ACPD
12, 17503–17538, 2012

3 Results

3.1 Experimental results

The spectral optical properties of aerosols were studied through the in situ observation of their scattering (σ_s) and absorption coefficients (σ_p) at three wavelengths in the visible range at the Rome Tor Vergata site. Daily average σ_s varied from 30 to 300 Mm^{-1}, and σ_p from 2 to 50 Mm^{-1} (single measurement reaching up to 800 Mm^{-1}, and 100 Mm^{-1}, respectively). From these, Scattering Angstrom Exponent ($SAE_{467–660}$), Absorption Angstrom Exponent ($AAE_{467–660}$), and Single Scattering Albedo (SSA_{467}, SSA_{530} and SSA_{660}) were derived (acronyms are summarized in Table 1). The analysis revealed some relations linking the $SAE_{467–660}$, the $AAE_{467–660}$, and the spectral variability of the SSA, i.e. $dSSA_{660–467} = SSA_{660} - SSA_{467}$.

In Fig. 1 we show the observed data (more than 15 500 data points) as $SAE_{467–660}$ (y axis) versus $dSSA_{660–467} \cdot AAE_{467–660}$ (x axis). Data are color coded by SSA_{530}. Since $AAE_{467–660}$ is always positive in the visible region (e.g Moosmüller et al., 2011), negative x values correspond to negative $dSSA_{660–467}$. This visualization highlights an inverse linear relation between $SAE_{467–660}$ and $dSSA_{660–467} \cdot AAE_{467–660}$.

Figure 2 shows the same data clustered by the $AAE_{467–660}$ (left column, panels a–e), and a subset of them color coded by N_7 (right column, panels f–l), when N_7 data were available. In particular, five separate subsets of the whole dataset are shown (figure rows): $SSA_{530} > 0.95$ (a,f), $0.9 < SSA_{530} < 0.95$ (b,g), $0.8 < SSA_{530} < 0.9$ (c,h), $0.7 < SSA_{530} < 0.8$ (d,i), $0.6 < SSA_{530} < 0.7$ (e,l). The $AAE_{467–660}$ color coded visualization (left column) highlights a strong correlation between the variables. The correlation coefficient (R^2) varies from 0.72 to 0.9. In general, the lower the $AAE_{467–660}$ and SSA_{530}, the larger the R^2.

Figure 2f–l (right column) shows that low SSA are mainly associated to large particle numbers, and viceversa. In urban areas, this is expected as high N_7 and low SSA are generally associated to polluted conditions, while clean conditions generally show

ACPD
12, 17503–17538, 2012

low N_7 and high SSA. ($SSA_{530} > 0.95$ (Fig. 2f) are dominated by $N_7 < 10000\,\#\,cm^{-3}$, $AAE_{467–660} > 2$ and $SAE_{467–660} < 2$. Conversely, $SSA_{530} < 0.8$ (Fig. 2i, l) are dominated by $N_{15} > 30000\,\#\,cm^{-3}$.) Note that the largest N_7 (red dots in Fig. 2h, i) are not associated to any $SAE_{467–660} > 2$ (Fig. 2g, h), a threshold that is conversely used to identify the optical dominance of fine particles. (In fact, $N_7 > 30000\,\#\,cm^{-3}$ with $SSA_{530} < 0.7$ (Fig. 2l) has $SAE_{467–660} < 1.8$ and $AAE_{467–660} < 2$, whilst $N_7 > 60000\,\#\,cm^{-3}$ (Fig. 2i) and $0.7 < SSA_{530} < 0.8$ has $SAE_{467–660} < 2$ and $AAE_{467–660} < 2$ (but $AAE_{467–660} > 2$ also).) These findings will be further discussed later in view of the simulation outcomes.

3.2 Numerical simulations

Numerical simulations of aerosol optical properties were performed to understand and interpret the experimental results presented in the previous section. To this purpose, we assumed the observed bulk aerosol properties (Fig. 1) to be the result of a combined effect of different aerosol populations, each of these dominating a specific particle size range and there described by a typical PNSD and a chemical composition (i.e., by a particle refractive index, $m(\lambda, D_p)$). The primary scope of this exercise was to evaluate the way each aerosol population affects the spectral variability of the bulk aerosol optical properties observed. Mie simulations of the aerosol scattering and absorption coefficients at three wavelengths (467, 530, 660 nm) were then performed, which required definition of a wavelength and size dependent refractive index, $m(\lambda, D_p) = m_{Re}(\lambda, D_p) - m_{Im}(\lambda, D_p)$.

Eight different aerosol populations were considered. Each of them covers a specific portion (60–120 nm, 120–300 nm, 300–800 nm, >800 nm) of the whole D_p size range considered (D_p from 20 nm to 10 µm). Two different sets of $m(\lambda, D_p)$ were used: they are intended to reproduce two extreme cases of low and high absorbtion, respectively. The average PNSDs used for the simulation were analyzed in a previous work (see Fig. 2 of Costabile et al., 2010), the daily average N_7 being from 3000 to $30\,000\,\#\,cm^{-3}$. The thresholds of the four D_p size regions were identified according to numerous previous

ACPD
12, 17503–17538, 2012

studies on urban aerosol PNSD modes (e.g. Costabile et al., 2009, and references therein). Overall, we used approximately 8300 PNSDs.

The eight different populations are summarized in the Table 2. In the D_p size range 60–120 nm we defined a "urban Aitken mode" (AM) and a "soot mode" (SM) using two sets of refractive indices to simulate slightly to highly absorbing particles. In the small accumulation mode size range (D_p = 120–300 nm) we included an organic mode, i.e. the "small OM condensation mode" (SOM), and a "Biomass Burning mode" (BBM). In the large accumulation mode range (D_p = 300–800 nm) we included conditions ranging from an inorganic aerosol mode (inorganic matter, IM, e.g. sulfates, in the droplet mode) referred to as " large IM accumulation mode" (LIM), and an organic aerosol mode, i.e. the "large OM accumulation mode" (LOM). Finally, in the coarse mode range (D_p = 0.8–10 µm), we simulated a "Marine coarse mode", MM (sea salts and OM) and a "Dust coarse mode" (DM).

Refractive indices $m(\lambda, D_p)$ were based on previous similar works (e.g. Kaufman et al., 2001; Dubovik et al., 2002; Bond and Bergstrom, 2006; Alexander et al., 2008; Moosmüller et al., 2009; Flowers et al., 2010; Cai et al., 2011). The choice of the spectrally dependent $m(\lambda, D_p)$ to employ was a challenging task, due to a still limited information available in the literature. Difficulties occurred in finding suitable $m_{Re}(\lambda, D_p)$ and $m_{Im}(\lambda, D_p)$ for all aerosol populations in Table 2: some of them (e.g. AM) have never been given a $m(\lambda, D_p)$, and some of them (e.g. DM) have been given several values in the literature. We therefore decided to fix a central value $\overline{m}(\lambda, D_p)$ and a range $\delta m(\lambda, D_p)$ in which we randomly varied $\overline{m}(\lambda, D_p)$. We then performed a sensitivity analysis of the calculated variables on the $m(\lambda, D_p) = \overline{m}(\lambda, D_p) \pm \delta m(\lambda, D_p)$. Calculations were carried out, in which both the real $m_{Re}(\lambda, D_p)$ and the imaginary $m_{Im}(\lambda, D_p)$ part of the complex $m(\lambda, D_p)$ were randomly varied between the extremes of $\overline{m}(\lambda, D_p) \pm \delta m(\lambda, D_p)$, namely $m_{Re} = \overline{m}_{Re} \pm \delta m_{Re}$ and $m_{Im} = \overline{m}_{Im} \pm \delta m_{Im}$, as shown in Table 2.

The simulated spectrally dependent aerosol scattering and absorption coefficients were combined to obtain, for every population, the $SAE_{467–660}$, $AAE_{467–660}$, $SSA_{467,530,660}$ and $dSSA_{660–467}$ parameters used in this study. These are shown as

ACPD
12, 17503–17538, 2012

a function of the D_p in Fig. 3. Calculations were carried out by using $\overline{m}(\lambda, D_p) = \overline{m_{Re}}(\lambda, D_p) - \overline{m_{Im}}(\lambda, D_p)$. Note that the discontinuity of the parameters in the four D_p regions selected is precisely the effect of the assumed size-dependent $m(\lambda, D_p)$. The effect of the $m(\lambda, D_p)$ variability within the same D_p size range (i.e., low- and high- absorbtion capabilities in the same D_p range, which means for example DM and MM) is conversely shown by the two thin lines, the solid one representing the average of the two.

As expected, the simulated $SAE_{467–660}$ (Fig. 3a) is generally low (<1) for aerosol dominated by the coarse particles, and large (>1) for aerosol dominated by the fine (i.e., the small accumulation mode) particles. However, it is worth noting that a decreasing $SAE_{467–660}$ with decreasing size is obtained in the Aitken mode range, reaching values similar to those typically attributed to coarse mode particles. This behavior is shown to be valid for both AM and SM populations. This aspect will be discussed in the following.

The simulated $AAE_{467–660}$ (Fig. 3b) shows a strong variability with both particle size and refractive index. $AAE_{467–660} < 2$ is mainly associated to SM,whilst $AAE_{467–660} > 2.5$ are found for the SOM, which was intended to simulate the dominance of brown carbon. The BBM simulation shows that $AAE_{467–660}$ increases with size.

The simulated SSA (Fig. 3c) is large (>0.9) and almost constant in the large accumulation mode, and decreases with both increasing (coarse mode) and decreasing (small accumulation and Aitken mode) diameters. The lowest SSA occurs for the blue and green wavelengths. Note that the lowest SSA (<0.5) is in the Aitken mode size range, where the spectral variability of SSA (in the blue and green) is the largest one. SSA_{660} shows a comparatively smaller decrease.

Coupling the results of $AAE_{467–660}$ and dSSA, their product $dSSA_{660–467} \cdot AAE_{467–660}$ (showed by the light-blue line in Fig. 3d together with $dSSA_{660–467}$ in black) is low in the accumulation mode and large in the coarse and Aitken mode size range, the latter case reaching the largest values. This behavior is thus opposite to that of $SAE_{467–660}$, and theoretically confirms the inverse relation experimentally observed between $SAE_{467–660}$

ACPD
12, 17503–17538, 2012

and $dSSA_{660-467} \cdot AAE_{467-660}$ (Fig. 1). Negative $dSSA_{660-467} \cdot AAE_{467-660}$ mainly result for the smaller diameters (120–250 nm) of BBM and the larger diameters (90–120 nm) of the AM. That is to say, $dSSA_{660-467} < 0$ is expected to be associated to aerosols dominated by either accumulation mode BC-rich combustion particles (for simplicity here referred to as BBM), or aged (some hours) urban particles (here referred to as AM in the 90–120 nm size range).

4 Discussion

4.1 A "paradigm" describing optical properties of aerosol populations

By combining the experimental results (Fig. 2) and the numerical simulations (Fig. 3) it is possible to explain the effects of key aerosol populations on the bulk intensive optical properties. This is shown in Fig. 4, built on the same variables of Fig. 1, and presenting the relation between $SAE_{467-660}$ and $dSSA_{660-467} \cdot AAE_{467-660}$ as obtained from the numerical simulation. The intensive parameters of the eight aerosol populations in Table 2 were calculated by integrating – for both cases of larger and lower $m_{Im}(\lambda, D_p)$ – the relevant extensive optical properties $\sigma_s(\lambda, D_p, N_{D_p})$ and $\sigma_p(\lambda, D_p, N_{D_p})$ over the four particle size ranges selected ΔD_p, and then calculating at the selected wavelengths $\Delta\lambda$ the intensive optical parameters $SAE(m, \Delta\lambda, \Delta D_p)$, $AAE(m, \Delta\lambda, \Delta D_p)$ and $dSSA(m, \Delta\lambda, \Delta D_p)$. To assess the robustness of the paradigm we show in the Fig. 4 both the calculations in which the central value $\overline{m}(\lambda, D_p) = \overline{m_{Re}}(\lambda, D_p) - \overline{m_{Im}}(\lambda, D_p)$ is used (large circles), and the calculations in which the $m(\lambda, D_p) = (\overline{m_{Re}}(\lambda, D_p) \pm \delta m_{Re}(\lambda, D_p)) - (\overline{m_{Im}}(\lambda, D_p) \pm \delta m_{Im}(\lambda, D_p))$ is used (small dots) (cf. Sect. 3.2) . More than 140 000 cases were calculated and their data points are showed in Fig. 4.

The resulting graph mirrors the experimentally observed graph in Fig. 1. "Regions" in which every single aerosol population – if alone – is expected to "move" the relation between $SAE_{467-660}$, and $dSSA_{660-467} \cdot AAE_{467-660}$ come out:

ACPD
12, 17503–17538, 2012

- coarse mode particles (DM and MM) lie in the region where $dSSA_{660-467} \cdot AAE_{467-660} > 0$, $SAE_{467-660} < 0.5$, and $SSA_{530} > 0.8$, DM having lower SSA_{530} and larger $dSSA_{660-467} \cdot AAE_{467-660}$ (absolute values) than MM has;
- large accumulation mode particles (LIM and LOM) are located in the area with $-0.01 < dSSA_{660-467} \cdot AAE_{467-660} < 0.07$, $0.5 < SAE_{467-660} < 3$, and $SSA_{530} > 0.9$, LOM having lower SSA_{530} and larger $dSSA_{660-467} \cdot AAE_{467-660}$ (absolute values) than LIM has;
- the small accumulation mode (BBM and SOM) drives data towards the area with $-0.05 < dSSA_{660-467} \cdot AAE_{467-660} < 0.1$, $SAE_{467-660} > 1.5$, and $SSA_{530} > 0.8$, BBM having lower SSA_{530} than SOM has;
- 60–120 nm particles (SM and AM) fall in the elongated blue and green area having $SSA_{530} < 0.8$, SM tending towards $SAE_{467-660} < 0.5$ and $0.1 < dSSA_{660-467} \cdot AAE_{467-660} < 0.3$, and AM towards $1 < SAE_{467-660} < 2.5$ and $-0.1 < dSSA_{660-467} \cdot AAE_{467-660} < 0.1$.

Overall, further relevant "directions" appear:

- an increased absorption tends to decrease $SAE_{467-660}$ and increase $dSSA_{660-467} \cdot AAE_{467-660}$ (absolute value);
- a change in D_p results in a decrease of $SAE_{467-660}$ in the case of both large D_p (coarse mode) and small D_p (SM and AM), the smaller particles (AM and SM) mode being separated from the coarse mode by its lower SSA_{530} (note that the largest $SAE_{467-660}$ occurs for fine (SOM and LIM) particles);
- $dSSA_{660-467}$ is determined by the comparison between $AAE_{467-660}$ and $SAE_{467-660}$, with $dSSA_{660-467} < 0$ for $AAE_{467-660} < SAE_{467-660}$, and $dSSA_{660-467} > 0$ for $AAE_{467-660} > SAE_{467-660}$.

ACPD
12, 17503–17538, 2012

4.2 Intensive optical properties observed for the key aerosol populations

Results in Fig. 4 suggest the existence of a general paradigm to separate the observed aerosol populations. The combination of the paradigm with the measurements can both tune up the paradigm and unravel the observations. Table 3 presents a re-analysis of the measurements (Fig. 2) in that context showing up the relevant intensive optical properties resulting for the key urban aerosol populations.

Overall, the populations with a larger $m_{\mathrm{lm}}(\lambda, D_{\mathrm{p}})$ (see Table 2) are separated in two regions by the threshold of $\mathrm{AAE}_{467\text{–}660} = 2$. In the region with $\mathrm{AAE}_{467\text{–}660} > 2$ (Fig. 2a–c and f–h) the absorption is dominated by SOM, LOM and DM. In this region, SOM, LOM, and DM are clearly separated by their $\mathrm{SAE}_{467\text{–}660}$ decreasing with increasing D_{p} (cf. Fig. 3a). SOM, which is intended to represent organic compounds (may include nitrates) in the "condensation mode", is found in Fig. 2a, b (and Fig. 2f, g) for $\mathrm{SAE}_{467\text{–}660} > 1.5$ and $\mathrm{AAE}_{467\text{–}660} > 2.5$. LOM (Fig. 2a, b, and equivalent Fig. 2f, g) and DM (Fig. 2b, c and equivalent Fig. 2g, h) are found in the same region of $\mathrm{AAE}_{467\text{–}660} > 2$ for $0.5 < \mathrm{SAE}_{467\text{–}660} < 2$ and $\mathrm{SAE}_{467\text{–}660} < 0.5$, respectively. In the same region of $\mathrm{AAE}_{467\text{–}660} > 2$ both MM and LIM lie (Fig. 2a, and equivalent Fig. 2f), the two aerosol populations having the lowest $m_{\mathrm{lm}}(\lambda, D_{\mathrm{p}})$.

$\mathrm{AAE}_{467\text{–}660} < 2$ highlights a region where SM and BBM are the dominant light absorbing components of the aerosol. Despite their similarities, SM and BBM are separated by the paradigm. SM appears in the panels d,e (and equivalent i, l) of Fig. 2 for $\mathrm{SAE}_{467\text{–}660} < 1$ and $\mathrm{dSSA}_{660\text{–}467} \cdot \mathrm{AAE}_{467\text{–}660} > 0.5$. BBM appears conversely in the panels c, d, e and equivalent h, i, l of Fig. 2 for $\mathrm{SAE}_{467\text{–}660} > 1$, and $\mathrm{dSSA}_{660\text{–}467} \cdot \mathrm{AAE}_{467\text{–}660} < 0.5$. Their different SSA_{530} results also in Fig. 3c, SSA of SM being smaller. They also show different $\mathrm{dSSA}_{660\text{–}467}$, SM having larger and positive $\mathrm{dSSA}_{660\text{–}467} \cdot \mathrm{AAE}_{467\text{–}660}$ (Fig. 3d). In fact, they represent aerosol populations with different chemical and physical properties, as well as light absorbing properties (e.g. Han et al., 2010). SM is intended to represent carbonaceous particles formed as combustion byproducts consisting of both BC and OC; those particles vary in the particle

ACPD
12, 17503–17538, 2012

size range of 30–200 nm mainly in the Aitken mode, and show complex mixing state in the atmosphere (e.g. Seinfeld and Pandis, 2006). BBM is intended to represent a BC-rich aerosol generated through the burning of vegetation long-range transported from far emission sources; BBM is generally in the 150–400 nm particle size range (e.g. Clarke et al., 2007). Note that BBM and SM represent particular cases of the "real" soot and biomass burning aerosols: in real cases both the D_p and the OM content can vary. In fact, the closer to the emission points, the smaller the D_p of both SM and BBM: this should translates into lower $SAE_{467–660}$, $AAE_{467–660}$ and SSA_{530} (see Fig. 3a–c). Conversely, the more aged is the aerosol, the larger the D_p: this should move e.g. the BBM towards the LOM in the Fig. 4 and should translate into lower $SAE_{467–660}$. As well, the larger the OM content of the combustion by-products (the D_p size range being the same), the larger the $AAE_{467–660}$ and $SAE_{467–660}$: this should result in BBM "moving" towards SOM, and SM towards AM in Fig. 4.

$SAE_{467–660}$ of SM can be as low (<1) as $SAE_{467–660}$ of DM. $SAE_{467–660} < 1$, generally attributed to coarse particles, can therefore also represent aerosols dominated by soot mode particles. Despite their similar $SAE_{467–660}$ as well as their similar $dSSA_{660–467} \cdot AAE_{467–660}$ (Fig. 3a, d), SM and DM are however separated by their different SSA_{530}, DM having $SSA_{530} > 0.85$ and SM having $SSA_{530} < 0.85$. Note that (Fig. 3) DM shows SSA_{530} decreasing and $dSSA_{660–467} \cdot AAE_{467–660}$ increasing with increasing D_p. Reversely, SM shows SSA_{530} decreasing and $dSSA_{660–467} \cdot AAE_{467–660}$ increasing with decreasing D_p. These tendencies are on the basis of the inverse relationship found between $SAE_{467–660}$ and $dSSA_{660–467} \cdot AAE_{467–660}$ in Fig. 1.

Both SM and AM (UFPs) show rather low $SAE_{467–660}$ (<1 for SM, and <2 for AM). This should result from the combination of the absorbing nature of those particles ($m_{Im}(\lambda, D_p) > 0$) coupled to their small D_p. Assuming no absorbtion for AM ($m_{Im}(\lambda, D_p) = 0$), Mie calculations translates to $SAE_{467–660} = 4$ (Rayleight scattering regime). We conversely simulated AM to have $m_{Im}(\lambda, D_p) > 0$, slightly varying with varying λ. The $m_{Im}(\lambda, D_p) > 0$ is intended to represent their likely content of OM, which has been argued to be more than 20 % in the urban background (Pohjola et al., 2007). The

ACPD
12, 17503–17538, 2012

light variability with λ of $m_{\mathrm{Im}}(\lambda, D_{\mathrm{p}})$ is intended to represent that this OM is not the refractory organic carbon typical of some biomass burning aerosols (Clarke et al., 2007). This assumption was corroborated by our experimental observations: AM shows up in Fig. 2c, d, e (and equivalent Fig. 2h, i, l), the $\mathrm{AAE}_{467-660}$ of AM dominated aerosols being $\leqq 2$.

SM and AM dominated aerosols (UFPs) show rather low SSA_{530}. Although expected for the soot (SM) (e.g. Moffet and Prather, 2009), this result might be atypical for AM. In fact, the numerical simulation (Fig. 3c) shows that SSA_{530} (and SSA_{467}) sharply decreases in the Aitken mode size range as a function of particle size, this affecting both the SM and the AM results. The change may be even stronger in the "real" atmosphere, where changes in particle size are associated with changes in chemical composition, and mixing state. Conversely, the numerical simulation hypothesizes a fixed chemical composition (that is a fixed $m(\lambda, D_{\mathrm{p}})$) for a given aerosol population size range.

The $\mathrm{AAE}_{467-660}$ of SM dominated aerosols (Fig. 2d, e) is >1 (it varies from 1 to 1.5). This is likely because our site is reached by soot shortly aged in the atmosphere (less than 1 h) rather than fresh soot, the aged soot containing more OM (e.g. Moffet and Prather, 2009). We therefore simulated SM (Table 2) by a $m_{\mathrm{Im}}(\lambda, D_{\mathrm{p}})$ smaller than values usually found in the literature (e.g. Alexander et al., 2008), which further refer to individual soot carbon particles rather then to bulk atmospheric aerosols like in our case. This observation makes the simulation of SM possible by the Mie theory, the aged soot being supposed to have a quite spherical shape.

4.3 Comparison to previous works

In this section we compare our findings to previous works. The aim is to demonstrate the general validity of the relations observed (the paradigm in Fig. 4) that puts these into a broader framework. The comparison with previous measurements is possible as the intensive aerosol parameters addressed do not strictly depend on local conditions (e.g. number concentrations, scattering and absorption coefficients).

ACPD
12, 17503–17538, 2012

In Fig. 5 we attempt a comparison between the paradigm in Fig. 4 and the observations taken during major field campaigns summarized in Table 4. Figure 5 shows a nice agreement. (Note that shaded areas in Fig. 5 sketch the simulation results of Fig. 4, and that the color of the points in Fig. 5 is coded according to SSA_{530} as in Fig. 4.) Among others, biomass burning observed in African Savana and Zambia (case 1 in Fig. 5 and Table 4), in Southern Africa during SAFARI (case 2), and in Asia during the EAST-AIRE (case 4) are shown to match quite well the direction of the BBM simulations. Urban industrial and mixed aerosol in Greenbelt, USA (case 3), aerosol mixed downwind of the US Atlantic coast during ICARTT (case 5), urban-industrial mixed aerosols in Mexico City measured by remote sensing (case 6) and in situ (case 7), pollution aerosols with high sulfate content (case 13) are shown to fall between the regions of LIM, LOM and AM, which are typical of urban areas. In the coarse mode, the desert dust and oceanic aerosol in Capeverde (case 8), and the Saharan dust during PRIDE (case 10) are shown to fit the region between DM and MM. The cases of dust + urban + industrial during ACE-Asia (case 9) and BC + dust sampled in Mexico City during MILAGRO (case 11) match quite well the SM and DM approximations.

The cases from 15 to 19 were measured during this study (cf. Sect. 4.2) and are included for comparison. They are intended to address aerosol populations not shown in the previous cases 1–14. The cases 15 and 19 show aerosols dominated by SM particles as observed in the Fig. 2l (and equivalent Fig. 2d) for $SSA_{530} < 0.8$, $N_7 > 5 \times 10^4\,\#\,cm^{-3}$, and $SAE_{467–660} < 1$. The case 16 shows an urban aerosol with a dominant AM (large N_7, but low absorption coefficients σ_p, not shown here) as observed in the Fig. 2h (and equivalent Fig. 2c) for $N_7 > 7 \times 10^4\,\#\,cm^{-3}$, and $SAE_{467–660} \approx 1.5$. The cases 17 and 18 show aerosols dominated by SOM and LOM as observed in Fig. 2a, b (and Fig. 2f,g) for $AAE_{467–660} > 2.5$, $SAE_{467–660} > 1.5$, and $N_7 < 10^4\,\#\,cm^{-3}$.

Whilst agreeing with previous works, the paradigm in Fig. 4 puts the aerosol observations into a more general framework. It is the $SAE_{467–660}/AAE_{467–660}$ ratio determining $dSSA_{660–467}$, the relation being inversely linear ($dSSA_{660–467}$ increases with decreasing $SAE_{467–660}/AAE_{467–660}$). Aerosols show therefore $dSSA_{660–467} < 0$ if

ACPD
12, 17503–17538, 2012

$SAE_{467–660}/AAE_{467–660} > 1$, and vice versa $dSSA_{660–467} > 0$ if $SAE_{467–660}/AAE_{467–660} < 1$ (cf. Table 4).

Coarse particles and soot mode particles (SM) show invariably $dSSA_{660–467} > 0$ ($SAE_{467–660}/AAE_{467–660} < 1$). Conversely, accumulation mode particles show two different conditions: for larger BC content ($AAE_{467–660} < 2$, e.g. BBM) they show $dSSA_{660–467} < 0$ ($SAE_{467–660}/AAE_{467–660} > 1$); for larger OM contents ($AAE_{467–660} > 2$, e.g. SOM and LOM) they show $dSSA_{660–467} > 0$ ($SAE_{467–660}/AAE_{467–660} < 1$). The latter case goes along with the conclusion by Russell et al. (2010) that for biomass burning the BC should cause a $dSSA < 0$ (biomass burning in BBM), whereas the OM should be characterized by a $dSSA > 0$ (biomass burning in SOM). The authors analysed the case of Mexico aerosol sampled by a C-130 during the MILAGRO campaign, in which increasing organic mass fraction caused the slope of SSA with λ to change from negative to positive, and speculated that for biomass burning smoke the BC can outweigh the OM and produce $dSSA < 0$. Similarly, the aging of the aerosol can change its $SAE_{467–660}/AAE_{467–660}$ ratio. Albeit with obvious limitations, the paradigm might show these changes due to aging. The case of BBM aging towards LOM mentioned in the Sect. 4.2 translates into a lower $SAE_{467–660}$ and higher $AAE_{467–660}$ (and $dSSA_{660–467} > 0$). A similar result was also obtained by Müller et al. (2007) that found the EAE of forest-fire smoke decreasing for increasing transport time (and increasing effective radius).

The paradigm shows that $dSSA_{660–467} < 0$ (Fig. 4) can be attributed to both BBM (biomass burning) and AM (urban aerosols) in both cases occurring for $SSA_{530} < 0.9$. This result is supported by the observations (Fig. 2) showing no case of $dSSA < 0$ for $SSA_{530} > 0.95$ (Fig. 2a), and few cases of $dSSA < 0$ for $0.9 < SSA_{530} < 0.95$ (Fig. 2b). Observations highlight that most of the $dSSA < 0$ cases show $AAE_{467–660} < 2$. Similar results were also observed by Russell et al. (2010), that showed (Fig. 3 of their paper) that, for $SSA > 0.9$, SSA increases with wavelength ($dSSA > 0$) and with increasing AAE, dSSA being always positive but for $AAE = 1.4$ (the only case representing low AAEs).

ACPD
12, 17503–17538, 2012

Clearly, it appears the difficulty to rigorously evaluate the optical properties of the Aitken mode without accurate measurements of their size, refractive index and mixing state. Albeit with caution, the findings in Fig. 4 can however open to additional explanations of situations in which the contemporary observation of low SAEs and low SSAs was (probably erroneously) attributed to the coarse mode with limited consideration for the Aitken mode. The case 19 in Fig. 5 and Table 4 shows a similar situation with aerosol dominated by BC in the soot mode. It was possible to explain this case with $SAE_{467–660}$ measured being down to −0.5 and no dust at all on the basis of the paradigm in Fig. 4. Similar observations of BC pollution plumes with SAE below 1 are not new (Clarke et al., 2007; Raut et al., 2009; Doherty et al., 2005). Raut et al. (2009) observed unclear and contrasting results in a subway environment in a Paris railway station, with low SAE and small SSA during the train passage. The observations were attributed to both the presence of absorbing iron oxides and the internally generated BC from the degradation of carbonaceous brake components. Clarke et al. (2007) observed SAE of approximately 1 for some apparent pollution data (in the related Fig. 8) and concluded those pollution data to be exceptions, successively explained to be dust. Doherty et al. (2005) observed a composite relation from three in-situ research platforms during the ACE-ASIA campaign: aerosol dominated by pollution, sea-salt and dust showed SSA as low as 0.75, SAE being approximately 1. Unfortunately, we could not include those works in Fig. 5 because the relevant data did not contain all the necessary information to fill the paradigm. However, our work indicates that the re-analysis of similar situations in the proposed framework of Fig. 4 can provide quite robust explanations.

Through the combined analysis of the spectral optical properties (Fig. 4), the paradigm furthermore provides insights into aerosol particle size and chemical composition. The proposed paradigm may complete previous aerosol classifications based on SAE, AAE, and SSA in which unclear situations were found: it might help in separating polluted and clean days (e.g. Gyawali et al., 2012) and dust and polluted dust (e.g. Lee et al., 2012), or unraveling aerosol mixtures (e.g. Yang et al., 2009), or understanding

ACPD
12, 17503–17538, 2012

strange cases (e.g. Clarke et al., 2007), or revealing the contribution of absorption in classifying aerosol properties (e.g. Gobbi et al., 2007). It is worth mentioning that our paradigm still works with the often used extinction angstrom exponent (EAE) rather than SAE. Nevertheless, in that case the inverse relationship in Fig. 1 is less clear (and the correlation R^2 lower) because unlike the SAE, the $EAE_{467-660}$ still combines both scattering and absorption information, thus not exploiting the specific role of absorption and its full potential.

5 Conclusions

Spectral optical properties of aerosol particles contain an outstanding set of information on their size and composition. Extracting this piece of information is crucial to obtain an optical classification scheme of aerosol. This is the backdrop of this work, in which two years measurements of aerosol optical properties (scattering and absorption coefficients at blue, green and red wavelengths (λ)) were collected at a suburban background site (Rome, Italy), together with measurements of particle number size distributions. Size distribution measurements were coupled to relevant optical simulations (Mie theory) to highlight the relative contribution of particle size (D_p) and refractive index ($m(\lambda, D_p)$) on the bulk aerosol properties.

The results of the work proved useful to draw a general "paradigm" to classify aerosol types. The paradigm was based on aerosol spectral scattering and absorption, namely Scattering and Absorption Angstrom Exponents, SAE and AAE, and the spectral Single Scattering Albedo, dSSA. In the framework of this classification scheme, key atmospheric aerosol populations were optically identified including soot, urban Aitken mode particles, biomass burning, organic and inorganic particles, dust and marine aerosols. Conclusions drawn from these results highlight that:

– aerosol populations show distinctive combinations of SAE and dSSA · AAE, those variables being linked by an inverse linear relationship varying with varying SSA;

ACPD
12, 17503–17538, 2012

– aerosol populations exhibit a dSSA depending on the SAE/AAE ratio, with dSSA < 0 for SAE/AAE > 1 (e.g. biomass burning rich in black carbon), and dSSA > 0 for SAE/AAE < 1 (e.g. dust, and soot);

– increasing particle absorption decreases SAE, so that coarse (e.g. dust) and soot aerosols show SAE < 1, whilst accumulation mode aerosols show SAE > 1.5;

– alike soot, urban Aitken mode particles show an imaginary part of $m(\lambda, D_p)$ greater than 0 resulting in SSA < 0.8, whilst fine and coarse aerosols (including dust) show SSA > 0.8.

The work finally presented a comparison between the proposed aerosol classification scheme and observations taken during previous field campaigns, the comparison showing a strict agreement. This result indicates both the general validity of the proposed relationships, and the possibility to provide additional interpretations to previous and future works. Nevertheless, besides adding new relevant data, outcomes of this work may be important both to improve current parameterizations of climate models, and to provide a more accurate characterization of the atmospheric load of carbonaceous aerosols from satellite measurements.

Acknowledgements. The measurements of particle numbers were supported by the Italian Ministry of Health, and the Department of Epidemiology of the ASL RM/E in the framework of the project "Impact of atmospheric pollution by airports on citizens health". We also thank G. Cattani for his support.

References

Ackerman, P. and Toon, O. B.: Absorption of visible radiation in atmosphere containing mixtures of absorbing and nonabsorbing particles, Appl. Opt., 20, 3661–3668, 1981. 17507

Alexander, D. T. L., Crozier, P. A., and Anderson, J. R.: Brown carbon spheres in East Asian outflow and their optical properties, Science, 321, 833–835, 2008. 17506, 17512, 17518

ACPD

12, 17503–17538, 2012

Anderson, T. L. and Ogren, J. A.: Determining aerosol radiative properties using the TSI 3563 integrating nephelometer, Aerosol Sci. Tech., 29, 57–69, 1998. 17508
Andreae, M. O. and Gelencsér, A.: Black carbon or brown carbon? The nature of light-absorbing carbonaceous aerosols, Atmos. Chem. Phys., 6, 3131–3148, doi:10.5194/acp-6-3131-2006, 2006. 17506
Barnaba, F. and Gobbi, G. P.: Aerosol seasonal variability over the Mediterranean region and relative impact of maritime, continental and Saharan dust particles over the basin from MODIS data in the year 2001, Atmos. Chem. Phys., 4, 2367–2391, doi:10.5194/acp-4-2367-2004, 2004. 17508
Basart, S., Pérez, C., Cuevas, E., Baldasano, J. M., and Gobbi, G. P.: Aerosol characterization in Northern Africa, Northeastern Atlantic, Mediterranean Basin and Middle East from direct-sun AERONET observations, Atmos. Chem. Phys., 9, 8265–8282, doi:10.5194/acp-9-8265-2009, 2009. 17506
Bergstrom, R. W.: Extinction and absorption coefficients of the atmospheric aerosol as a function of particle size, Beitr. Phys. Atmos., 46, 223–234, 1973. 17507
Bergstrom, R. W., Russell, P. B., and Hignett, P.: Wavelength dependence of the absorption of black carbon particles: predictions and results from the TARFOX experiment and implications for the aerosol single scattering albedo, J. Atmos. Sci., 59, 567–577, 2002. 17507
Bergstrom, R. W., Pilewskie, P., Russell, P. B., Redemann, J., Bond, T. C., Quinn, P. K., and Sierau, B.: Spectral absorption properties of atmospheric aerosols, Atmos. Chem. Phys., 7, 5937–5943, doi:10.5194/acp-7-5937-2007, 2007. 17506, 17507
Bergstrom, R. W., Schmidt, K. S., Coddington, O., Pilewskie, P., Guan, H., Livingston, J. M., Redemann, J., and Russell, P. B.: Aerosol spectral absorption in the Mexico City area: results from airborne measurements during MILAGRO/INTEX B, Atmos. Chem. Phys., 10, 6333–6343, doi:10.5194/acp-10-6333-2010, 2010. 17533
Bond, T. C.: Spectral dependence of visible light absorption by carbonaceous particles emitted from coal combustion, Geophys. Res. Lett., 28, 4075–4078, 2001. 17506, 17508
Bond, T. C. and Bergstrom, R. W.: Light absorption by carbonaceous particles: an investigative review, Aerosol Sci. Tech., 40, 27–67, 2006. 17512
Bond, T. C., Anderson, T. L., and Campbell, D.: Calibration and intercomparison of filter-based measurements of visible light absorption by aerosols, Aerosol Sci. Tech., 30, 582–600, 1999. 17508, 17509

ACPD
12, 17503–17538, 2012

Bond, T. C., Covert, D. S., and Müller, T., Truncation and angular-scattering corrections for absorbing aerosol in the TSI 3563 nephelometer, Aerosol Sci. Tech., 43, 866–871, 2009. 17508

Cai, Y., Montague, D. C., and Deshler, T.: Comparison of measured and calculated scattering from surface aerosols with an average, a size-dependent, and a time-dependent refractive index, J. Geophys. Res., 116, D02202, doi:10.1029/2010JD014607, 2011. 17512

Cappa, C. D., Lack, D. A., Burkholder, J. B., and Ravishankara, A. R.: Bias in filter-based aerosol light absorption measurements due to organic aerosol loading: evidence from laboratory measurements, Aerosol Sci. Tech., 42, 1022–1032, 2008. 17509

Clarke, A., McNaughton, C., Kapustin, V., Shinozuka, Y., Howell, S., Dibb, J., Zhou, J., Anderson, B., Brekhovskikh, V., Turner, H., and Pinkerton, M.: Biomass burning and pollution aerosol over North America: organic components and their influence on spectral optical properties and humidification response, J. Geophys. Res., 112, D12S18, doi:10.1029/2006JD007777, 2007. 17507, 17517, 17518, 17521, 17522

Costabile, F., Birmili, W., Klose, S., Tuch, T., Wehner, B., Wiedensohler, A., Franck, U., König, K., and Sonntag, A.: Spatio-temporal variability and principal components of the particle number size distribution in an urban atmosphere, Atmos. Chem. Phys., 9, 3163–3195, doi:10.5194/acp-9-3163-2009, 2009. 17512

Costabile, F., Amoroso, A., and Wang, F.: Sub- m particle size distributions in a suburban Mediterranean area. Aerosol populations and their possible relationship with HONO mixing ratios, Atmos. Environ., 44, 5258–5268, 2010. 17509, 17511

Doherty, S. J., Quinn, P. K., Jefferson, A., Carrico, C. M., Anderson, T. L., and Hegg, D.: A comparison and summary of aerosol optical properties as observed in situ from aircraft, ship, and land during ACE-Asia, J. Geophys. Res., 110, D04201, doi:10.1029/2004jd004964, 2005. 17521

Dubovik, O., Holben, B., Eck, T. F., Smirnov, A., Kaufman, Y. J., King, M. D., Tanré, D., and Slutsker, I.: Variability of absorption and optical properties of key aerosol types observed in worldwide locations, J. Atmos. Sci., 59, 590–608, 2002. 17507, 17512, 17533

Flowers, B. A., Dubey, M. K., Mazzoleni, C., Stone, E. A., Schauer, J. J., Kim, S.-W., and Yoon, S. C.: Optical-chemical-microphysical relationships and closure studies for mixed carbonaceous aerosols observed at Jeju Island; 3-laser photoacoustic spectrometer, particle sizing, and filter analysis, Atmos. Chem. Phys., 10, 10387–10398, doi:10.5194/acp-10-10387-2010, 2010. 17512

ACPD
12, 17503–17538, 2012

Gobbi, G. P., Barnaba, F., and Ammannato, L.: The vertical distribution of aerosols, Saharan dust and cirrus clouds in Rome (Italy) in the year 2001, Atmos. Chem. Phys., 4, 351–359, doi:10.5194/acp-4-351-2004, 2004. 17508

Gobbi, G. P., Kaufman, Y. J., Koren, I., and Eck, T. F.: Classification of aerosol properties derived from AERONET direct sun data, Atmos. Chem. Phys., 7, 453–458, doi:10.5194/acp-7-453-2007, 2007. 17506, 17509, 17522

Gyawali, M., Arnott, W. P., Zaveri, R. A., Song, C., Moosmüller, H., Liu, L., Mishchenko, M. I., Chen, L.-W. A., Green, M. C., Watson, J. G., and Chow, J. C.: Photoacoustic optical properties at UV, VIS, and near IR wavelengths for laboratory generated and winter time ambient urban aerosols, Atmos. Chem. Phys., 12, 2587–2601, doi:10.5194/acp-12-2587-2012, 2012. 17507, 17521

Han, Y. M., Cao, J. J., Lee, S. C., Ho, K. F., and An, Z. S.: Different characteristics of char and soot in the atmosphere and their ratio as an indicator for source identification in Xi'an, China, Atmos. Chem. Phys., 10, 595–607, doi:10.5194/acp-10-595-2010, 2010. 17516

Holben, B. N., Eck, T. F., Slutsker, I., Tanre, D., Buis, J. P., Setzer, A., Vermote, E., Reagan, J. A., Kaufman, Y. J., Nakajima, T., Lavenu, F., Jankowiak, I., and Smirnov, A.: AERONET – a federated instrument network and data archive for aerosol characterization, Remote Sens. Environ., 66, 1–16, 1998. 17506

Hinds, W. C.: Aerosol Technology, 2nd edn., John Wiley and Sons, New York, 1999. 17509

Intergovernmental Panel on Climate Change: Fourth Assessment Report: Climate Change 2007: The AR4 Synthesis Report, Geneva: IPCC, available at: http://www.ipcc.ch/ipccreports/ar4-wg1.htm, last access: 3 August 2010, 2007. 17505

Kaufman, Y. J., Tanre, D., Dubovik, O., Karnieli, A., and Remer, L. A.: Absorption of sunlight by dust as inferred from satellite and ground-based remote sensing, Geophys. Res. Lett., 28, 1479–1482, 2001. 17507, 17512

Kirchstetter, T. W., Novakov, T., and Hobbs, P.: Evidence that the spectral dependence of light absorption by aerosols is affected by organic carbon, J. Geophys. Res., 109, D21208, doi:10.1029/2004JD004999, 2004. 17506

Kulmala, M., Asmi, A., Lappalainen, H. K., Baltensperger, U., Brenguier, J.-L., Facchini, M. C., Hansson, H.-C., Hov, Ø., O'Dowd, C. D., Pöschl, U., Wiedensohler, A., Boers, R., Boucher, O., de Leeuw, G., Denier van der Gon, H. A. C., Feichter, J., Krejci, R., Laj, P., Lihavainen, H., Lohmann, U., McFiggans, G., Mentel, T., Pilinis, C., Riipinen, I., Schulz, M., Stohl, A., Swietlicki, E., Vignati, E., Alves, C., Amann, M., Ammann, M., Arabas, S., Artaxo, P.,

ACPD
12, 17503–17538, 2012

Baars, H., Beddows, D. C. S., Bergström, R., Beukes, J. P., Bilde, M., Burkhart, J. F., Canonaco, F., Clegg, S. L., Coe, H., Crumeyrolle, S., D'Anna, B., Decesari, S., Gilardoni, S., Fischer, M., Fjaeraa, A. M., Fountoukis, C., George, C., Gomes, L., Halloran, P., Hamburger, T., Harrison, R. M., Herrmann, H., Hoffmann, T., Hoose, C., Hu, M., Hyvärinen, A., Hõrrak, U., Iinuma, Y., Iversen, T., Josipovic, M., Kanakidou, M., Kiendler-Scharr, A., Kirkevåg, A., Kiss, G., Klimont, Z., Kolmonen, P., Komppula, M., Kristjánsson, J.-E., Laakso, L., Laaksonen, A., Labonnote, L., Lanz, V. A., Lehtinen, K. E. J., Rizzo, L. V., Makkonen, R., Manninen, H. E., McMeeking, G., Merikanto, J., Minikin, A., Mirme, S., Morgan, W. T., Nemitz, E., O'Donnell, D., Panwar, T. S., Pawlowska, H., Petzold, A., Pienaar, J. J., Pio, C., Plass-Duelmer, C., Prévôt, A. S. H., Pryor, S., Reddington, C. L., Roberts, G., Rosenfeld, D., Schwarz, J., Seland, Ø., Sellegri, K., Shen, X. J., Shiraiwa, M., Siebert, H., Sierau, B., Simpson, D., Sun, J. Y., Topping, D., Tunved, P., Vaattovaara, P., Vakkari, V., Veefkind, J. P., Visschedijk, A., Vuollekoski, H., Vuolo, R., Wehner, B., Wildt, J., Woodward, S., Worsnop, D. R., van Zadelhoff, G.-J., Zardini, A. A., Zhang, K., van Zyl, P. G., Kerminen, V.-M., S Carslaw, K., and Pandis, S. N.: General overview: European Integrated project on Aerosol Cloud Climate and Air Quality interactions (EUCAARI) – integrating aerosol research from nano to global scales, Atmos. Chem. Phys., 11, 13061–13143, doi:10.5194/acp-11-13061-2011, 2011. 17505

Jacobson, M. Z.: Strong radiative heating due to the mixing state of black carbon in atmospheric aerosols, Nature, 409, 695–697, 2001. 17506

Lack, D. A., Cappa, C. D., Covert, D. S., Baynard, T., Massoli, P., Sierau, B., Bates, T. S., Quinn, P. K., Lovejoy, E. R., and Ravishankara, A. R.: Bias in filter-based aerosol light absorption measurements due to organic aerosol loading: evidence from ambient measurements, Aerosol Sci. Tech., 42, 1033–1041, 2008. 17509

Lee, S., Yoon, S. C., Kim, S. W., Kim, Y. P., Ghim, Y. S., Kim, J. H., Kang, C. H., Kim, Y. J., Chang, L. S., and Lee, S. J.: Spectral dependency of light scattering/absorption and hygroscopicity of pollution and dust aerosols in Northeast Asia, Atmos. Environ., 50, 246–254, 2012. 17507, 17521, 17533

Moffet R. C. and Prather, K. A.: In-situ measurements of the mixing state and optical properties of soot with implications for radiative forcing estimates, Proc. Natl. Acad. Sci., 106, 11872–11877, 2009. 17518

ACPD
12, 17503–17538, 2012

Moosmüller, H., Chakrabarty, R. K., and Arnott, W. P.: Aerosol light absorption and its measurement: a review, J. Quant. Spectrosc. Ra., 110, 844–878, doi:10.1016/j.jqsrt.2009.02.035, 2009. 17506, 17512

Moosmüller, H., Chakrabarty, R. K., Ehlers, K. M., and Arnott, W. P.: Absorption Ångström coefficient, brown carbon, and aerosols: basic concepts, bulk matter, and spherical particles, Atmos. Chem. Phys., 11, 1217–1225, doi:10.5194/acp-11-1217-2011, 2011. 17510, 17534

Müller, D., Mattis, I., Ansmann, A., Wandinger, U., Ritter, C., and Kaiser, D.: Multiwavelength Raman lidar observations of particle growth during long-range transport of forest-fire smoke in the free troposphere, Geophys. Res. Lett., 34, L05803, doi:10.1029/2006GL027936, 2007. 17520

Müller, T., Laborde, M., Kassell, G., and Wiedensohler, A.: Design and performance of a three-wavelength LED-based total scatter and backscatter integrating nephelometer, Atmos. Meas. Tech., 4, 1291–1303, doi:10.5194/amt-4-1291-2011, 2011. 17508

O'Neill, N. T., Dubovik, O., and Eck, T. F.: A modified Ångstrom coefficient for the characterization of sub-micron aerosols, Appl. Opt., 40, 2368–2375, 2001a. 17506

O'Neill, N. T., Eck, T. F., Holben, B. N., Smirnov, A., and Dubovik, O.: Bimodal size distribution influences on the variation of Angstrom derivatives in spectral and optical depth space, J. Geophys. Res., 106, 9787–9806, 2001b. 17506

Pohjola, M. A., Pirjola, L., Karppinen, A., Härkönen, J., Korhonen, H., Hussein, T., Ketzel, M., and Kukkonen, J.: Evaluation and modelling of the size fractionated aerosol particle number concentration measurements nearby a major road in Helsinki – Part I: Modelling results within the LIPIKA project, Atmos. Chem. Phys., 7, 4065–4080, doi:10.5194/acp-7-4065-2007, 2007. 17517

Raut, J. C., Chazette, P., and Fortain, A.: Link between aerosol optical, microphysical and chemical measurements in an underground railway station in Paris, Atmos. Environ., 43, 860–868, 2009. 17521

Reche, C., Querol, X., Alastuey, A., Viana, M., Pey, J., Moreno, T., Rodríguez, S., González, Y., Fernández-Camacho, R., de la Rosa, J., Dall'Osto, M., Prévôt, A. S. H., Hueglin, C., Harrison, R. M., and Quincey, P.: New considerations for PM, Black Carbon and particle number concentration for air quality monitoring across different European cities, Atmos. Chem. Phys., 11, 6207–6227, doi:10.5194/acp-11-6207-2011, 2011. 17505

Russell, P. B., Bergstrom, R. W., Shinozuka, Y., Clarke, A. D., DeCarlo, P. F., Jimenez, J. L., Livingston, J. M., Redemann, J., Dubovik, O., and Strawa, A.: Absorption Angstrom Exponent

ACPD
12, 17503–17538, 2012

in AERONET and related data as an indicator of aerosol composition, Atmos. Chem. Phys., 10, 1155–1169, doi:10.5194/acp-10-1155-2010, 2010. 17506, 17507, 17520, 17533
Seinfeld, J. H. and Pandis, S. P.: Atmospheric Chemistry and Physics, 2nd edn., John Wiley, New York, USA, 1232 pp., 2006. 17505, 17517
Subramanian, R., Roden, C. A., Boparai, P., and Bond, T. C.: Yellow beads and missing particles: trouble ahead for filterbased absorption measurements., Aerosol Sci. Tech., 41, 630–637, 2007. 17509
Sun, H., Biedermann, L., and Bond, T. C.: Color of brown carbon: a model for ultraviolet and visible light absorption by organic carbon aerosol, Geophys. Res. Lett., 34, L17813, doi:10.1029/2007GL029797, 2007. 17506
UNEP: Integrated Assessment of Black Carbon and Tropospheric Ozone, Summary for Decision Makers, United Nations Environment Program and World Meteorological Organization, UNEP/GC/26/INF/20, Nairobi, Kenya, 2011. 17505
Yang, M., Howell, S. G., Zhuang, J., and Huebert, B. J.: Attribution of aerosol light absorption to black carbon, brown carbon, and dust in China – interpretations of atmospheric measurements during EAST-AIRE, Atmos. Chem. Phys., 9, 2035–2050, doi:10.5194/acp-9-2035-2009, 2009. 17507, 17521, 17533
Virkkula, A.: Correction of the calibration of the 3-wavelength Particle Soot Absorption Photometer (3λPSAP), Aerosol Sci. Tech., 44, 706–712, 2010. 17508
Virkkula, A., Ahlquist, N. C., Covert, D. S., Arnott, W. P., Sheridan, P. J., Quinn, P. K., and Coffman, D. J.: Modification, calibration and a field test of an instrument for measuring light absorption by particles, Aerosol Sci. Tech., 39, 68–83, 2005. 17508, 17509
WHO: Health Aspects of Air Pollution with Particulate Matter, Ozone and Nitrogen Dioxide, Report on a WHO Working Group, Bonn, Germany, 13–15 January 2003, WHO, Regional Office for Europe, Copenhagen, 2003. 17505

ACPD
12, 17503–17538, 2012

Table 1. Acronyms.

Symbol	Meaning	Description
AAE	Absorption Angstrom Exponent	
AM	Aitken mode	Urban Aitken mode particles generated by growing of nucleation mode particles. (AM might include some condensation mode particles)
BBM	Biomass Burning Mode	Small accumulation mode particles rich in BC from biomass burning.
BC	Black Carbon	
DM	Dust Mode	Coarse mode dust particles
dSSA	$dSSA_{660–467}$	SSA_{660}–SSA_{467}
LIM	Large inorganic mode	Large accumulation mode particles rich in inorganic matter (e.g., sulphates, sea salts).
LOM	Large organic mode	Large accumulation mode particles rich in OM.
MM	Marine mode	Coarse mode particles in the marine aerosol rich in sea salt and OM.
N	Total particle number	
OM	Organic Material	
SAE	Scattering Angstrom Exponent	
SM	Soot Mode	Soot mode particles generated as combustion byproducts consisting of both BC and OM.
SOM	Small Organic Mode	Condensation mode particles rich in OM (SOM might include both urban and biomass burning aerosol particles).
SSA	Single Scattering Albedo	

ACPD
12, 17503–17538, 2012

Table 2. Aerosol populations (A.P.) used for the numerical simulations. Particle size ranges (D_p), and refractive index ($m(\lambda, D_p) = m_{Re}(\lambda, D_p) - m_{Im}(\lambda, D_p)$) are indicated. For the sensitivity analysis $m = (\overline{m_{Re}} \pm \delta m_{Re}) - (\overline{m_{Im}} \pm \delta m_{Im})$, δm being the range of random variation around the central value $\overline{m}$.

A.P.	D_p (nm)	$\overline{m}(\lambda, D_p) = \overline{m_{Re}}(\lambda, D_p) - \overline{m_{Im}}(\lambda, D_p)$ $\lambda = 467$ nm	$\lambda = 530$ nm	$\lambda = 660$ nm	δm_{Re}	δm_{Im}
AM	60–120	1.426 – 0.008*i*	1.424 – 0.005*i*	1.425 – 0.006*i*	±0.01	±0.001
SM	60–120	1.520 – 0.047*i*	1.520 – 0.047*i*	1.520 – 0.047*i*	±0.01	±0.001
SOM	120–300	1.5 – 0.02*i*	1.486 – 0.011*i*	1.496 – 0.012*i*	±0.01	±0.001
BBM	120–300	1.512 – 0.027*i*	1.510 – 0.021*i*	1.511 – 0.022*i*	±0.01	±0.001
LIM	300–800	1.43 – 0.00002*i*	1.43 – 0.00001*i*	1.429 – 0.000013*i*	±0.01	±0.0001
LOM	300–800	1.460 – 0.012*i*	1.454 – 0.008*i*	1.512 – 0.0075*i*	±0.01	±0.001
MM	>800	1.550 – 0.00019*i*	1.550 – 0.00006*i*	1.550 – 0.00011*i*	±0.01	±0.0001
DM	>800	1.560 – 0.008*i*	1.550 – 0.004*i*	1.560 – 0.005*i*	±0.01	±0.001

ACPD
12, 17503–17538, 2012

Table 3. Intensive optical properties (SSA, SAE, AAE, and dSSA) of key aerosol populations (A.P.) resulting from the work, and related total particle number concentration (N).

A.P.	SSA_{530}	$SAE_{467-660}$	$AAE_{467-660}$	$dSSA_{660-467}$	N_7 ($\#cm^{-3}$)
AM	<0.8	1–2.5	≈2	−0.1–0.1	$>5 \times 10^4$
SM	<0.8	<1	<1.5	0.1–0.3	$>5 \times 10^4$
SOM	>0.85	1.5–3	>2.5	0–0.1	$<2 \times 10^4$
BBM	<0.85	1–3	<2	−0.1–0.05	$<2 \times 10^4$
LIM	>0.95	0.5–3	≈2.5	0–0.01	$<10^4$
LOM	>0.9	0.5–2	>2.5	0–0.1	$<10^4$
MM	>0.95	<0.5	>2	0–0.05	$<10^4$
DM	>0.85	<0.5	≈2	0.05–0.3	$<10^4$

ACPD
12, 17503–17538, 2012

Table 4. Observations of aerosol populations (A.P.) considered for the comparison to the aerosol classification paradigm drawn in Fig. 5. (Numbers in Fig. 5 represent the ID showed here.)

ID	A.P.	Description	Observations	Reference
1	BBM	African Savana	Remote sensing	Dubovik et al. (2002)
2	BBM	SAFARI,Southern Africa, biomass smoke	Remote sensing	Russell et al. (2010)
3	mixed	Urban-industrial-mixed, Greenbelt93-00	Remote sensing	Dubovik et al. (2002)
4	BBM	EAST AIRE, biomass burning	In-situ	Yang et al. (2009)
5	mixed	ICARTT, downwind of US coast urban aerosols	Remote sensing	Russell et al. (2010)
6	mixed	Urban-industrial-mixed, Mexico City	Remote sensing	Dubovik et al. (2002)
7	mixed	MILAGRO, flights over Mexico City, BC+OM	In-situ	Bergstrom et al. (2010)
8	MM+DM	Desert dust-Oceanic, Cape verde	Remote sensing	Dubovik et al. (2002)
9	mixed	ACE Asia, Dust-urban-industrial	Remote sensing	Russell et al. (2010)
10	DM	PRIDE, Saharan dust	Remote sensing	Russell et al. (2010)
11	mixed	MILAGRO, flights over Mexico City, BC+Dust	In-situ	Bergstrom et al. (2010)
12	LOM+LIM	Pollution 1 (higher OC/EC ratio)	In-situ	Lee et al. (2012)
13	LIM+mixed	Pollution 2 (higher nss-sulfate/EC ratio)	In-situ	Lee et al. (2012)
14	DM+LOM	Pollution + Dust	In-situ	Lee et al. (2012)
15	SM+mixed	Urban + downwind of soot emissions from aircraft	In-situ	This work
16	AM+mixed	Urban pollution + aitken mode	In-situ	This work
17	LOM	Scattering accumulation mode particles	In-situ	This work
18	SOM+LOM	Organic accumulation mode particles	In-situ	This work
19	SM	Urban soot mode	In-situ	This work

ACPD
12, 17503–17538, 2012

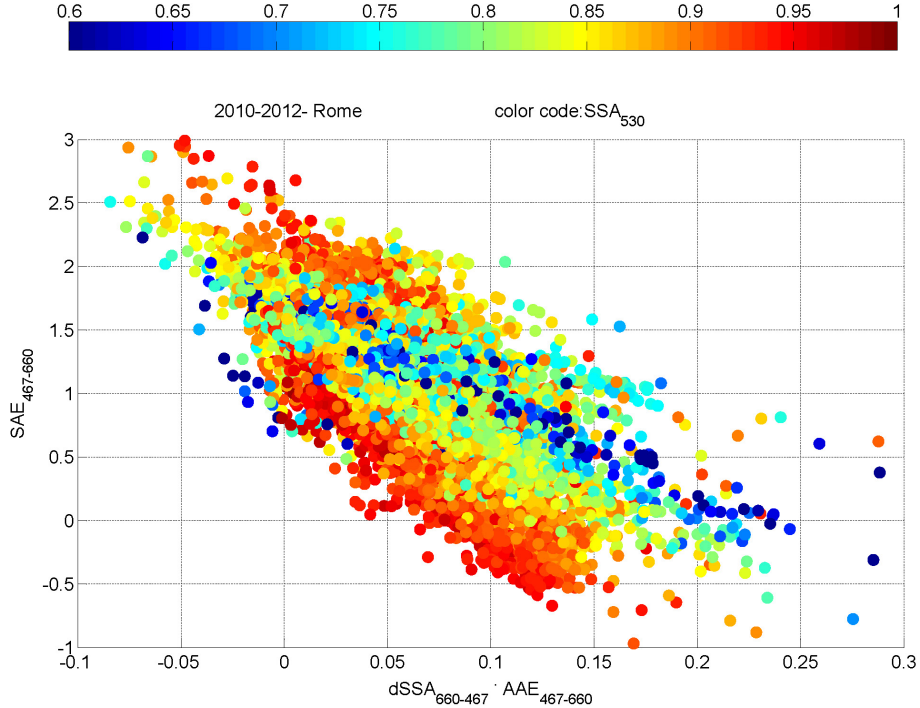

Fig. 1. Inverse linear relation observed between SAE and dSSA · AAE. The slope varies with varying SSA (color code). Note that since $AAE_{467–660}$ is always positive in the visible region (e.g. Moosmüller et al., 2011), negative *x* values correspond to negative $dSSA_{660–467}$.

ACPD
12, 17503–17538, 2012

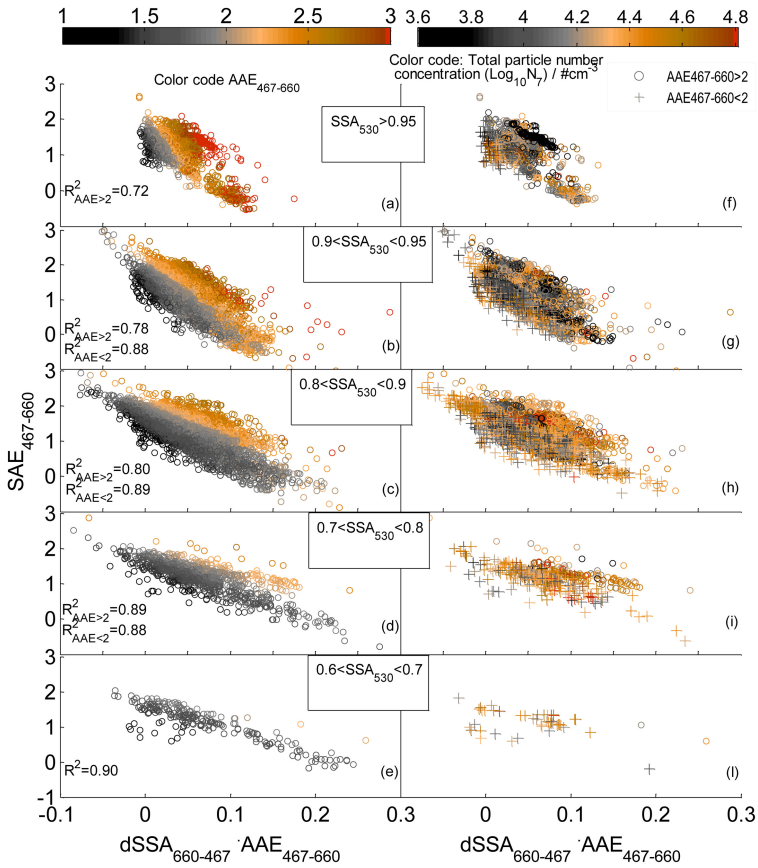

Fig. 2. As in Fig. 1, but data separated in terms of: (i) SSA (by row, same SSA in **a**/**f**, **b**/**g**, **c**/**h**, **d**/**i**, **e**/**l**), (ii) AAE (color code of the left column, **a, b, c, d, e**), and (iii) total particle number concentration, N (color code of the right column, **f, g, h, i, l**). R^2 = correlation coefficients between SAE and dSSA · AAE separately showed for AAE < 2 and AAE > 2. Note that R^2 varies with varying SSA and AAE.

ACPD
12, 17503–17538, 2012

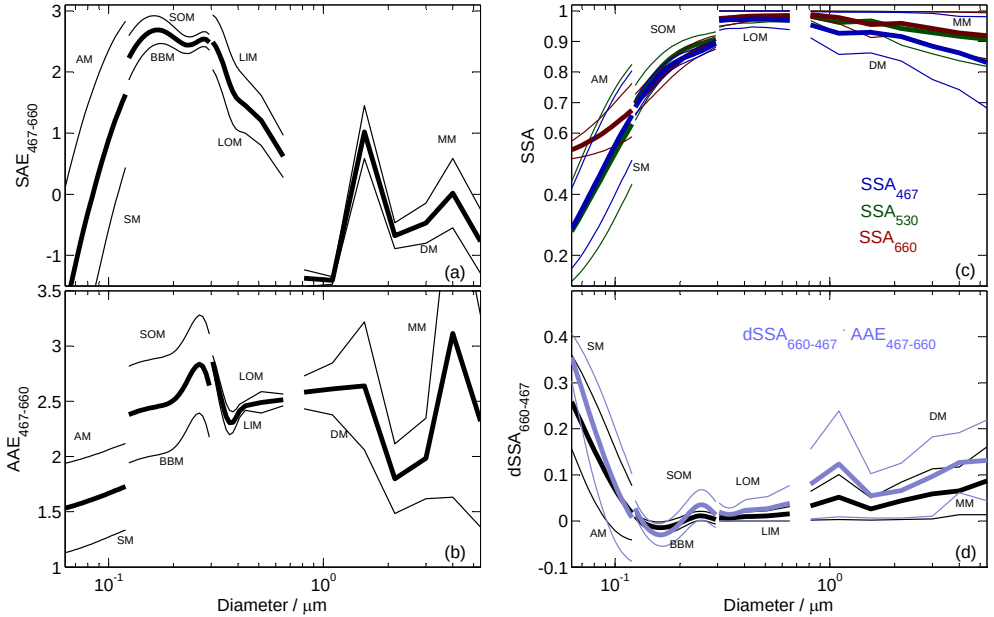

Fig. 3. Numerical simulations (Mie theory) of intensive optical properties: **(a)** SAE, **(b)** AAE, **(c)** SSA (at blue, green, and red wavelengths), **(d)** dSSA (black line), and dSSA · AAE (cyan line). Variables are numerically resolved by particle diameter D_p (x axis) and refractive index $\overline{m}(\lambda, D_p)$. Light lines represent the $\overline{m}(\lambda, D_p)$ variability between two extremes whose average value is showed by the thick lines. Note that the variables identify eight aerosol populations indicated by their acronyms (Table 1).

ACPD
12, 17503–17538, 2012

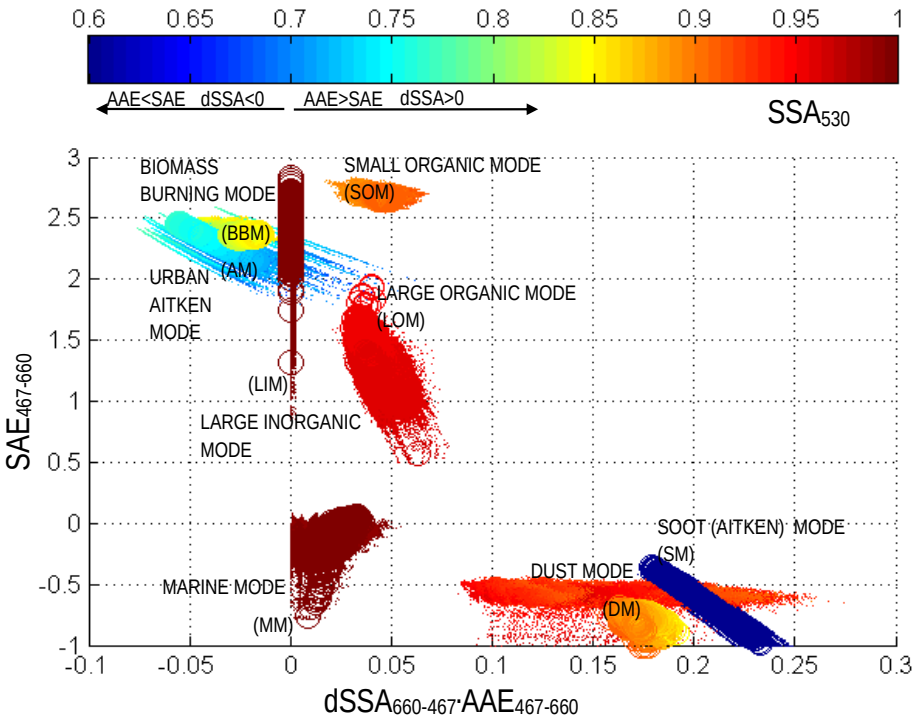

Fig. 4. Results of the numerical simulations illustrating the "paradigm" proposed to classify aerosol populations. Note that large-circle-dots show calculations with refractive index $m = \overline{m}(\lambda, D_p)$, and point-dots with the $m = \overline{m}(\lambda, D_p) \pm \delta m(\lambda, D_p)$ used for the sensitivity analysis.

ACPD
12, 17503–17538, 2012

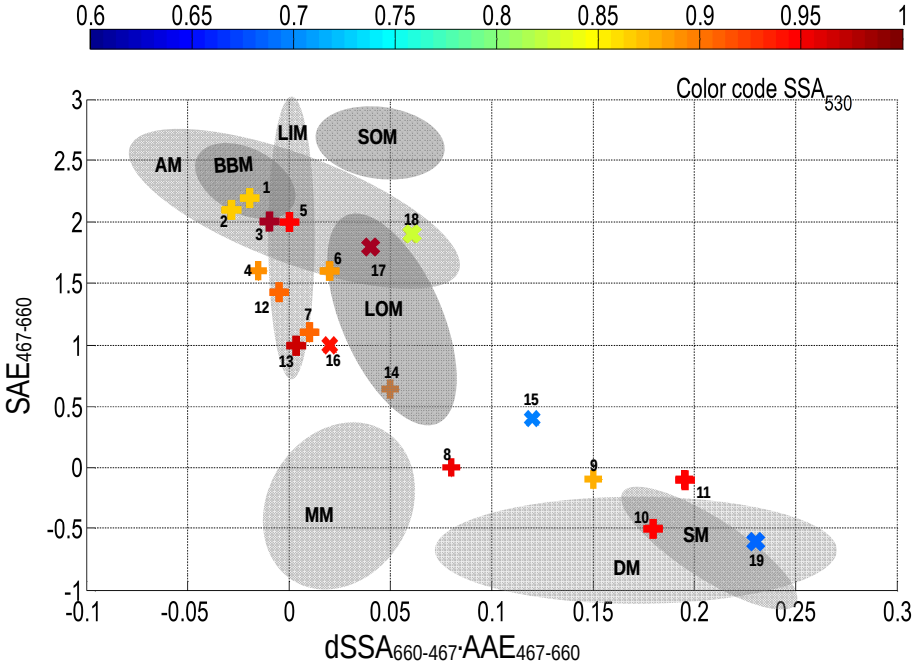

Fig. 5. Comparison between the aerosol classification paradigm proposed and observations taken during previous field campaigns (Table 4). The symbols "+" indicate previous observations, and the "×" indicate observations from this work, both of them being color coded by SSA. Note that shaded areas intend to reproduce the numerical results showed in Fig. 4.

ACPD
12, 17503–17538, 2012